ATMOSPHERIC DYNAMICS

Large-scale self-organization in dry turbulent atmospheres

Alexandros Alexakis[1]*, Raffaele Marino[2], Pablo D. Mininni[3], Adrian van Kan[4], Raffaello Foldes[2], Fabio Feraco[2,5]

How turbulent convective fluctuations organize to form larger-scale structures in planetary atmospheres remains a question that eludes quantitative answers. The assumption that this process is the result of an inverse cascade was suggested half a century ago in two-dimensional fluids, but its applicability to atmospheric and oceanic flows remains heavily debated, hampering our understanding of the energy balance in planetary systems. We show using direct numerical simulations with spatial resolutions of $12288^2 \times 384$ points that rotating and stratified flows can support a bidirectional cascade of energy, in three dimensions, with a ratio of Rossby to Froude numbers comparable to that of Earth's atmosphere. Our results establish that, in dry atmospheres, spontaneous order can arise through an inverse cascade to the largest spatial scales.

Flow structures thousands of kilometers wide are not uncommon in the atmosphere of Earth and that of other planets. The energy of these structures could originate from processes associated with the global atmospheric circulation but could also originate from smaller-scale convective turbulence. In the latter case, small-scale eddies conspire to self-organize into larger structures. Such a process goes against our daily life experience, where turbulence generates smaller-scale erratic structures, such as those observed when pouring milk into a cup of coffee. It is therefore necessary to come up with convincing mechanisms for how such large-scale organization can take place in planetary atmospheres.

One of the most important theoretical discoveries in the 20th century in the field of nonequilibrium physics is the phenomenon of self-organization, which spontaneously creates large-scale order out of small-scale disorder. One of the first examples of this process was given by Onsager with the statistical mechanics of a gas of point vortices (*1*) that was later generalized to two-dimensional (2D) turbulent flows (*2*–*5*). A 2D flow conserves an additional invariant, the enstrophy, given by the mean squared vorticity. The relation between energy and enstrophy leads to an incompatibility for the simultaneous bulk transfer of both quantities to the small scales. As a result, vortices self-interact, transferring enstrophy to smaller scales, whereas energy is transferred to larger scales. This process takes place on a continuum of scales, forming a constant flux of energy from small to large scales in what is known as an inverse energy cascade, as opposed to the disordered forward energy cascade observed in 3D turbulence that is directed to small scales.

Although planetary atmospheres are often very thin (Earth's atmosphere has horizontal synoptic scales of the order of 1000 km and a pressure scale height of 7.6 km), the corresponding flows are far from being 2D. Nonetheless, two-dimensionality is not imperative for the appearance of self-organization. 3D rotating and stratified flows (two key ingredients of atmospheric dynamics) conserve a different invariant—the potential vorticity—that can also lead to an inverse cascade. This happens in the quasi-geostrophic limit, where rotation and stratification are asymptotically strong (*6*) and where gravito-inertial waves are filtered out. Inverse cascades can also be present in rotating Rayleigh-Bénard convection (*7*–*11*), where in this case, a generalized quasi-geostrophic limit can be considered that partially preserves gravito-inertial modes. However, for most planetary flows, the quasi-geostrophic limit is, at best, a crude approximation, with gravito-inertial waves composing a substantial part of the energy budget cascading energy forward (*12*–*15*). Thus, an inverse cascade in planetary atmospheres caused either by two-dimensionality or quasi-geostrophy remains conjectural.

Could atmospheric dynamics display an inverse cascade away from these limits? In recent years it has been demonstrated that a hybrid state can be reached such that larger scales cascade energy inversely, whereas smaller scales cascade energy forward in what is now known as a bidirectional cascade (*16*). Bidirectional cascades were observed early on with direct numerical simulations (DNS) (*17*–*22*). In rotating and stratified flows, simulations indicate the presence of bidirectional cascades (*23*–*25*), though in a regime where rotation and stratification are comparable in strength, which is typical for the ocean but not for the atmosphere.

Nonetheless, the existence of self-organization processes through a bidirectional cascade in planetary atmospheres has become a compelling possibility as recent research using satellite images with cloud tracking analysis and in situ aircraft measurements has estimated the flux (and thus also the direction) of the energy cascades in planetary flows in Earth's atmosphere (*26*, *27*), the ocean (*28*), and the Jovian atmosphere (*11*, *29*). These studies have affirmed the presence of both inverse and forward energy cascades depending on the scale examined or on the altitude. However, satellite images constrain the measurements to 2D slices, thus ignoring any processes occurring in the third direction.

Up to now, there is no definite evidence of whether planetary atmospheric flows satisfy the necessary conditions for a bidirectional cascade to establish itself. The difficulty in answering such questions lies, on the one hand, in the fact that information from satellite images is limited and, on the other hand, in the extreme parameter values that are met in planetary atmospheres, which are hard to obtain in DNS. However, not only has the technology to perform high-cadence high-resolution observations of the atmosphere just started to come along, but the computational power to perform DNS of stratified atmospheres in a realistic parameter space has also become available. In this work, with the use of DNS in a large grid using 40,000,000 central processing unit (CPU) hours, we establish that the fluid model of a rotating and stably stratified dry atmosphere described by the nonhydrostatic Boussinesq equations can generate a bidirectional cascade leading to large-scale organization of the flow.

Set up

We consider a fluid in a Cartesian, triply periodic domain of vertical height H and horizontal dimension $L = 32H$, in the presence of gravity, a stable mean density gradient, and solid body rotation in the vertical direction (*30*). The dynamics of the system are described by the incompressible velocity field $\mathbf{u}$ and the normalized density variation ϕ, governed by the Boussinesq equations (*31*, *32*)

$$\partial_t \mathbf{u} + \mathbf{u}\cdot\nabla\mathbf{u} + 2\boldsymbol{\Omega}\times\mathbf{u} = -\nabla P - \mathbf{e_z} N\phi + \nu\nabla^2\mathbf{u} + \mathbf{f} \quad (1)$$

$$\partial_t \phi + \mathbf{u}\cdot\nabla\phi = N\mathbf{e_z}\cdot\mathbf{u} + \kappa\nabla^2\phi \quad (2)$$

where $\boldsymbol{\Omega}$ is the solid body rotation rate, N is the Brunt-Väisälä frequency, P is the pressure, ν is the viscosity, κ is the density diffusivity, and $\mathbf{f}$ is an external forcing acting at scales

[1]Laboratoire de Physique de l'Ecole normale supérieure, ENS, Université PSL, CNRS, Sorbonne Université, Université Paris-Diderot, Sorbonne Paris Cité, Paris, France. [2]Université de Lyon, CNRS, École Centrale de Lyon, INSA Lyon, Université Claude Bernard Lyon 1, Laboratoire de Mécanique des Fluides et d'Acoustique, UMR5509 - F-69134, Écully, France. [3]Universidad de Buenos Aires, Facultad de Ciencias Exactas y Naturales, Departamento de Física, and CONICET - Universidad de Buenos Aires, Instituto de Física Interdisciplinaria y Aplicada (INFINA), Ciudad Universitaria, 1428 Buenos Aires, Argentina. [4]Department of Physics, University of California Berkeley, Berkeley, CA 94720, USA. [5]Leibniz-Institute of Atmospheric Physics at the University of Rostock, 18225 Kühlungsborn, Germany.
*Corresponding author. Email: alexakis@phys.ens.fr

$\ell_F \sim H$ injecting energy at a rate ϵ. Although this model has some strong simplifications, like periodicity or a simplified forcing mechanism, it is the most elementary model capturing the necessary physics to reproduce atmospheric dynamics.

This system has four independent nondimensional control parameters: (i) the Reynolds number $Re_\epsilon = \epsilon^{1/3} k_H^{-4/3}/\nu$; (ii) the Prandtl number $Pr = \nu/\kappa$, that here is set to unity; (iii) the Rossby number $Ro_\epsilon = \epsilon^{1/3} k_H^{2/3}/\Omega$; and (iv) the Froude number $Fr_\epsilon = \epsilon^{1/3} k_H^{2/3}/N$ (with $k_H = 2\pi/H$). We can also define dimensionless parameters based on the domain size L and the flow root mean square velocity U as, for example, $Re = UL/\nu$, $Ro = U/(H\Omega)$, and $Fr = U/(NH)$, which are closer to the definitions used in atmospheric measurements.

Simulations were performed at resolutions of $12288^2 \times 384$ grid points (*30*, *33*). As a reference, a domain height H = 15 km (equal to twice the pressure scale height in Earth's atmosphere) corresponds to a domain length of 480 km (corresponding to atmospheric mesoscales) and a vertical and horizontal resolution of 39 m. Our simulations are characterized by $Re_\epsilon = 2000$, $Ro_\epsilon = 1$, and $Fr_\epsilon = 0.025$, or alternatively $Re \approx 2 \times 10^6$, $Ro \approx 0.4$, and $Fr \approx 0.01$. These values are also compatible, for example, with that of the mesosphere–lower thermosphere (MLT) (*34*).

Results

Figure 1 shows visualizations of the flow and the density field made using VAPOR (*35*). Structures with horizontal widths 10 times as large as that of H can be seen by visual inspection. At the same time, looking at the zoomed-in cross sections, it is obvious that these structures are far from being 2D. In the larger scales, pancake structures of alternating sign of ϕ along the vertical and the emergence of macroscopic cyclones and anticyclones are visible in Fig. 1 (top right). These features are observed in weather maps and are a landmark of larger-scale, energy-containing structures in Earth's atmosphere. At the same time, smaller-scale overturning events can be seen in the zoomed-in section that are one-tenth the size of H (Fig. 1, bottom right) and are also detectable sometimes in the sky as Kelvin-Helmholtz billows. Thus, even at this qualitative level, the presence of a bidirectional cascade is evident.

To become more quantitative, we note that the inviscid Boussinesq equations conserve the total energy $\mathcal{E}_T$ given by the sum of kinetic energy $\mathcal{E}_K$ and potential energy $\mathcal{E}_P$. Alternatively we decomposed it into the energy of gravito-inertial modes $\mathcal{E}_{GW}$ and the energy of quasi-geostrophic modes $\mathcal{E}_{QG}$, where $\mathcal{E}_T = \mathcal{E}_{GW} + \mathcal{E}_{QG}$. Gravito-inertial modes are dispersive wave modes due to the combined restoring force of gravity and Coriolis, whereas quasi-geostrophic modes balance Coriolis and gravity forces with pressure (see materials and methods for their exact definitions). These energies are distributed differently in the Fourier space, among vertical wave numbers $k_\parallel$ and horizontal wave numbers $k_\perp$. We define three different energy spectra averaged over fixed $k_\parallel$, $k_\perp$, and $k = \sqrt{k_\parallel^2 + k_\perp^2}$. We do not define a new symbol for each spectrum but distinguish between them by their argument—i.e., $E_i(k)$, $E_i(k_\perp)$, and $E_i(k_\parallel)$ where i is T, K, P, GW, or QG, which stand for total, kinetic, potential, gravito-inertial wave, and quasi-geostrophic, respectively. In addition, we define $E_i(k_\perp, k_\parallel)$ that shows the spectral energy density for a given pair $k_\perp, k_\parallel$.

The left panels in Fig. 2 show the energy spectra $E_i(k)$, $E_i(k_\perp)$, and $E_i(k_\parallel)$ with the energy component i as indicated in the legend. The inset also shows the ratios $R_{GW} = E_{GW}/E_T$ and $R_{QG} = E_{QG}/E_T$. In the top panel, for $k > k_H$, the spectra have been averaged over shells of width k_H because otherwise large peaks of period k_H are observed due to the strong domain anisotropy, shown by the light gray lines for the total energy spectrum. For wave numbers larger than k_H and smaller than the viscous wave number k_ν, the spherically averaged spectrum displays a power-law behavior with an exponent very close to Kolmogorov's prediction $k^{-5/3}$ for homogeneous isotropic turbulence. This power-law behavior, composed 70% by gravito-inertial waves, is indicative of a forward energy cascade. At k smaller than k_H, a similar power law is observed (albeit with a smaller prefactor). This indicates the presence of an inverse cascade. This energy at small k is almost exclusively kinetic, dominated by 2D quasi-geostrophic modes.

For $E_i(k_\perp)$, three different power laws can be observed. First, in the range $k_L < k_\perp < k_H$, a $k_\perp^{-5/3}$ law is observed, where $k_L = 2\pi/L$. This is consistent with Earth's atmospheric spectrum between ≈10 and 500 km (*36*). Second, in the range $k_H < k_\perp < k_B = N/U$, a steeper power law close to $k_\perp^{-3}$ is observed, where k_B is the buoyancy wave number. Finally, at larger $k_\perp$, a shallower power-law slope starts to appear with exponent close to −5/3. Finally, the last panel of Fig. 2 shows $E_i(k_\parallel)$ with $k^{-5/3}$ and k^{-3} power laws indicated as references, the latter observed in the atmosphere at vertical scales near 1 km caused by gravity waves (*37*).

The right panels of Fig. 2 show the energy fluxes across different surfaces in wave number space: across constant k spheres $\Pi_i(k)$, constant $k_\perp$ cylinders $\Pi_i(k_\perp)$, and constant $k_\parallel$ planes $\Pi_i(k_\parallel)$. As with the spectra, we distinguish between fluxes based on their arguments. Here, i is T, K, or P, which stand for total, kinetic, and potential energies, respectively. Positive values imply a flux of energy toward larger wave numbers, whereas negative values indicate a flux toward smaller wave numbers. $\Pi_T(k)$ flux is positive for $k > k_H$, which indicates a forward cascade. However, a small fraction, corresponding to 5% of the total energy injection rate, cascades toward larger scales. This is seen in the negative flux observed at $k < k_H$. This flux is also constant for more than a decade of wave numbers almost up to k_L. The inset in Fig. 2 shows the amplitude of this negative flux measured from different simulations varying only Re. The flux

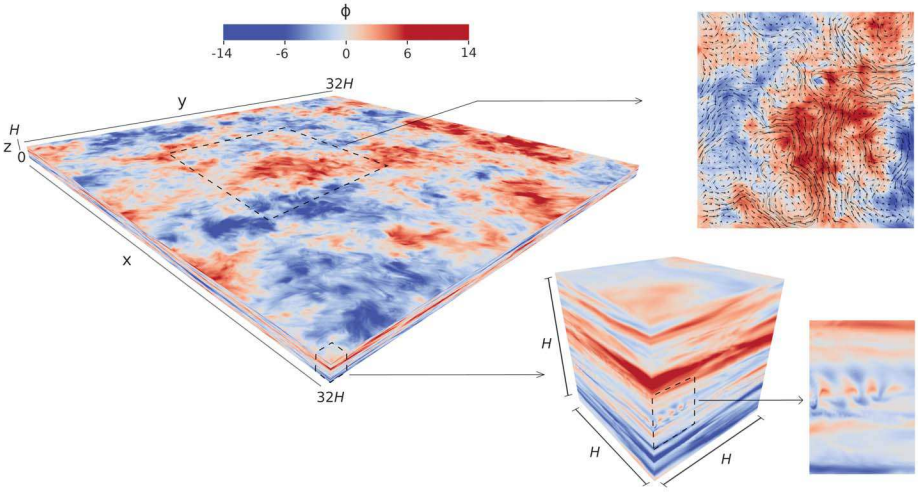

Fig. 1. Visualization of density fluctuations φ and of the velocity field in the computational domain. Structures at scales much larger than the forcing (i.e., at the scale of the domain height, with wave number $k_F = 2\pi/H$) are abundant in the visible horizontal plane (left), indicative of an efficient transfer of the energy toward the lowest modes along the perpendicular direction in Fourier space. The large-scale patterns are visible in the flow visualization, shown by arrows in a zoomed-in view (top right). At the same time, 3D instability patterns and small-scale features are detectable in both horizontal and vertical cuts of the zoomed-in simulation domain (bottom right), which suggests the action of a forward turbulent cascade. See the supplementary materials for a movie of the density fluctuations in the entire domain. Visualizations were done with VAPOR (*35*).

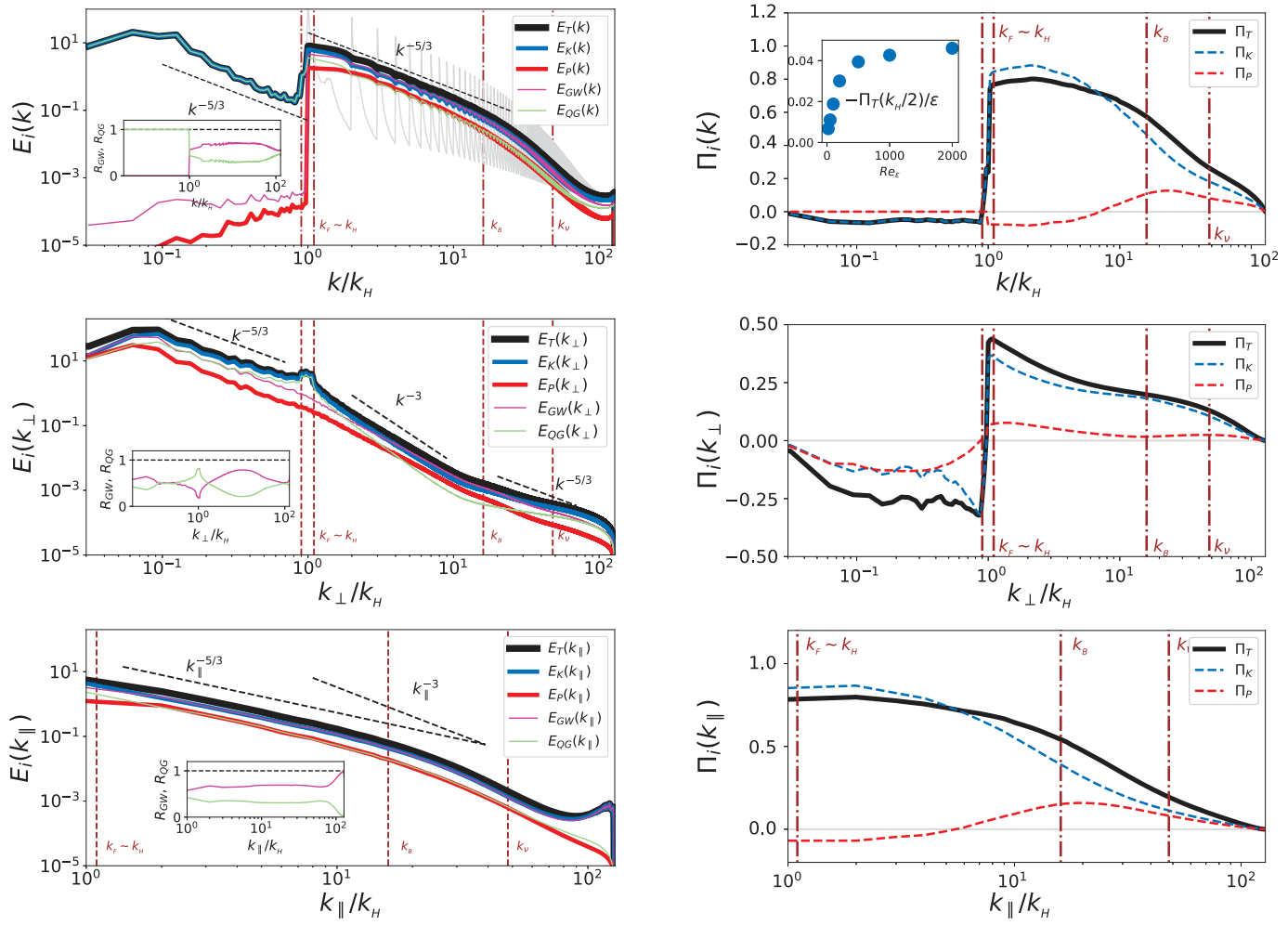

Fig. 2. Energy spectra and fluxes. (Left) Spherically (top), cylindrically (middle), and plane (bottom) averaged energy spectra, for all energy components. Insets show the ratios of energy components $R_{GW} = E_{GW}/E_T$ (pink) and $R_{QG} = E_{QG}/E_T$ (green). (Right) Energy fluxes across spheres (top), cylinders (middle), and planes (bottom) in spectral space. Total energy flux (black line), energy flux of kinetic energy (blue line), and energy flux of potential energy (red line) are shown. The forcing wave number $k_F \approx k_H$ (where energy is injected), the buoyancy wave number $k_B = N/U$, and the dissipation wave number k_ν (where energy is dissipated) are indicated by vertical dashed lines.

increases with *Re* and saturates at the largest *Re*. $\Pi_T(k_\perp)$ is also positive for $k_\perp > k_H$ and negative for $k_\perp < k_H$. However, in this case, the fraction of energy that cascades toward smaller $k_\perp$ is five times as large as $\Pi_T(k)$. $\Pi_T(k_\parallel)$ is positive everywhere.

Although in 1D spectra and fluxes it is easier to identify power laws, the energy distribution depends on $k_\parallel$ and $k_\perp$ independently. In Fig. 3, we show color-shaded plots of $E_T(k_\perp, k_\parallel)$ and $R_{GW} = E_{GW}(k_\perp,k_\parallel)/E_T(k_\perp,k_\parallel)$. The arrows indicate the direction of the energy transfers based on the fluxes in Fig. 2. A part of the injected energy is transferred to larger $k_\perp$ (purple arrows), producing the $k_\perp^{-3}$ spectrum observed in the $k_H < k_\perp < k_B$ range. $R_{GW}(k_\perp, k_\parallel)$ indicates that this forward transfer takes place through GW modes (green arrow). The peak of $E(k_\perp, k_\parallel)$ is observed at $k_\perp \simeq 2k_L$ and $k_\parallel \simeq 2k_H$, formed by an inverse transfer indicated by the black arrow and dominated by QG modes. This energy is responsible for the formation of the $k_\perp$ scaling at small $k_\perp$ in Fig. 2. When rotation-dominated scales are reached at $2\Omega k_\parallel \simeq Nk_\perp$ (black dotted line), QG modes transfer their energy to GW modes that cascade it back to small scales. Of the energy that has moved to smaller $k_\perp$, a finite amount is transferred (cyan arrow) below the smallest dashed white line ($k_\perp^2 + k_\parallel^2 = k_H^2$). The energy in these modes forms the $E(k) \propto k^{-5/3}$ spectrum for $k < k_H$. This component of the energy is the only one that escapes to the largest scales $k \to 0$ and corresponds to a true inverse cascade.

Conclusions

We have shown that dry turbulent atmospheres modeled by the nonhydrostatic Boussinesq equations can lead to a bidirectional energy cascade. The results showed that there is a flux of energy directed to the small wave numbers *k*, corresponding to 5% of the total energy injection rate at the largest Reynolds number. This flux, albeit small, is shown to persist up to the largest scales of the system and is *Re*-independent as large values of *Re* are reached.

Our analysis provides a detailed description of how energy is transferred across scales and between different modes. These transfers, indicated by the arrows sketched in Fig. 3, summarize the results in this work. Stratification, rotation, and the geometric constraint of finite *H* all play a role in the formation of this inverse cascade. In physical terms, at the scale of the forcing, stratification is dominant, constraining a large fraction of the energy to QG modes. This leads to the formation of pancake structures, known in stratified turbulence (*38*), that move energy to smaller $k_\perp$ and larger $k_\parallel$. This process ceases at wave numbers where stratification is comparable to rotation, $Nk_\perp \propto 2\Omega k_\parallel$. Rotation, which tends to bidimensionalize the flow (*39*), prevents larger $k_\parallel$ modes from appearing, and energy is converted to gravito-inertial mode energy that cascades back to

larger k. This is true for all k except for the $k_{\parallel}$ = 0 modes that are unaffected by rotation. These modes, which follow 2D dynamics, cascade the energy to ever smaller $k_{\perp}$. Their stability against 3D perturbations is assured by rotation and the finiteness of H that leads to the $k_{\parallel}$ = 0 modes being isolated (*16*). As a result, they cascade energy to ever smaller $k_{\perp}$ with no channel to return this energy back to the small scales.

An important outcome from this picture is that energy fluxes obtained from horizontal averages can significantly overestimate the inverse energy flux. In the presently examined simulation, $\Pi_T(k_{\perp})$ was five times as large as the true inverse flux $\Pi_T(k)$. This result limits the observational estimates of $\Pi_T(k)$. Most present estimates of the inverse flux are based on averages of 2D slices obtained by satellite images. They thus contain no information on the fields' variations in the third direction, and as a result, it is $\Pi_T(k_{\perp})$ that is measured and not $\Pi_T(k)$, which represents the true inverse flux. As a reference, and for comparisons with observations, we provide as supplementary materials [fig. S1 (*30*)] spectra and third-order structure functions along horizontal tracks, such as those resulting from airplane or satellite measurements. The structure functions display a change in sign indicative of an inverse cascade but overestimate the inverse flux, just as horizontal averages do. Thus, these estimates of the inverse flux could be significantly larger than their true values.

Although our model is not designed to capture the full complexity of Earth's atmosphere, which also has energy sources at planetary scales larger than our computational domain, it reproduces some known features in the mesoscale range. Global models indicate that the atmospheric spectrum varies with altitude, with observations showing that planetary and synoptic scales follow a k^{-3} spectrum at scales larger than 500 km. This is attributed to a direct cascade originating at planetary scales, which are not part of our domain. At scales smaller than 500 km, which are considered in our model, and down to ≈10 km, the observed spectrum follows $k^{-5/3}$ scaling, which agrees with our simulation. The dynamics producing this observed scaling, and whether it originates from a forward or an inverse cascade, have been long debated (*40*). An inverse cascade acting on those scales was proposed as an explanation (*41*, *42*), but it was later discarded (*23*, *40*) because purely stratified turbulence develops no inverse cascade. Our simulation shows that the combination of a realistic aspect ratio with realistic parameters gives rise to upscaling of energy with a $k^{-5/3}$ spectrum even at scales as small as 15 km. Although weak, the persistence of the inverse cascade makes a few percent of the flux enough to account for the observed mesoscale energy (*42*). But unlike the transfer to gravity waves hypothesized by Lilly (*42*), the inverse transfer we observe feeds the QG modes. At even smaller scales (<10 km), model parameterizations and the lack of observations with simultaneous high spatial coverage and resolution, especially in the upper atmosphere, prevent us from drawing definitive conclusions about spectral slopes and their origins. The spectrum in this range is still anisotropic, displays variability, and is sensitive to atmospheric conditions and to the local energy dissipation rate (*43*). It is difficult to make direct comparisons with the simulation in this range, but some common features can be identified, such as the prevalence of gravity waves and the occurrence of two horizontal Kolmogorov subranges above 10 km and below 1 km with different amplitudes mediated by a steeper spectrum, as has sometimes been reported in observational campaigns (*43*, *44*). Our work presents a spectral energy distribution from the mesoscales down to the smallest turbulent scales as a direct outcome of the physical mechanisms in the model and the parameter range examined. As such, it provides a link between theory and field observations that can help validate or discard theoretical explanations.

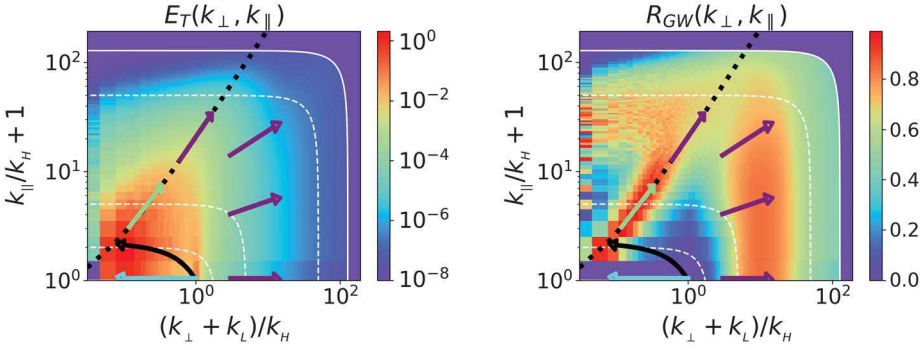

Fig. 3. 2D energy spectra in log-log scale. White dashed lines indicate isotropic contours (i.e., modes with constant wave number k). The solid white line indicates the maximum resolved wave numbers. (Left) Total energy spectrum. (Right) Gravity wave energy spectrum ratio. The black dotted lines marks $2\Omega k_{||} = Nk_{\perp}$, where inertial wave frequency matches gravity wave frequency. The arrows indicate the direction of the flux of energy (see text for a description).

REFERENCES AND NOTES

1. L. Onsager, *Nuovo Cim.* **6**, 279–287 (1949).
2. R. H. Kraichnan, *Phys. Fluids* **10**, 1417–1423 (1967).
3. R. H. Kraichnan, D. Montgomery, *Rep. Prog. Phys.* **43**, 547–619 (1980).
4. C. E. Leith, *Phys. Fluids* **11**, 671–672 (1968).
5. G. K. Batchelor, *Phys. Fluids* **12**, II-233–II-239 (1969).
6. J. G. Charney, *J. Atmos. Sci.* **28**, 1087–1095 (1971).
7. P. H. Roberts, *Philos. Trans. Royal Soc. A* **263**, 93–117 (1968).
8. F. H. Busse, *J. Fluid Mech.* **44**, 441–460 (1970).
9. A. M. Rubio, K. Julien, E. Knobloch, J. B. Weiss, *Phys. Rev. Lett.* **112**, 144501 (2014).
10. B. Favier, L. J. Silvers, M. R. E. Proctor, *Phys. Fluids* **26**, 096605 (2014).
11. L. Siegelman *et al.*, *Nat. Phys.* **18**, 357–361 (2022).
12. J. Vanneste, I. Yavneh, *J. Atmos. Sci.* **61**, 211–223 (2004).
13. J. Vanneste, *Annu. Rev. Fluid Mech.* **45**, 147–172 (2013).
14. J. Thomas, D. Daniel, *J. Fluid Mech.* **911**, A60 (2021).
15. J. Thomas, D. Daniel, *J. Fluid Mech.* **902**, A7 (2020).
16. A. Alexakis, L. Biferale, *Phys. Rep.* **767–769**, 1–101 (2018).
17. L. M. Smith, J. R. Chasnov, F. Waleffe, *Phys. Rev. Lett.* **77**, 2467–2470 (1996).
18. A. Celani, S. Musacchio, D. Vincenzi, *Phys. Rev. Lett.* **104**, 184506 (2010).
19. K. Seshasayanan, S. J. Benavides, A. Alexakis, *Phys. Rev. E* **90**, 051003 (2014).
20. S. J. Benavides, A. Alexakis, *J. Fluid Mech.* **822**, 364–385 (2017).
21. A. Sozza, G. Boffetta, P. Muratore-Ginanneschi, S. Musacchio, *Phys. Fluids* **27**, 035112 (2015).
22. A. van Kan, A. Alexakis, *J. Fluid Mech.* **899**, A33 (2020).
23. R. Marino, P. D. Mininni, D. Rosenberg, A. Pouquet, *Europhys. Lett.* **102**, 44006 (2013).
24. A. Pouquet, R. Marino, *Phys. Rev. Lett.* **111**, 234501 (2013).
25. R. Marino, A. Pouquet, D. Rosenberg, *Phys. Rev. Lett.* **114**, 114504 (2015).
26. D. Byrne, J. A. Zhang, *Geophys. Res. Lett.* **40**, 1439–1442 (2013).
27. G. P. King, J. Vogelzang, A. Stoffelen, *J. Geophys. Res. Oceans* **120**, 346–361 (2015).
28. D. Balwada, J.-H. Xie, R. Marino, F. Feraco, *Sci. Adv.* **8**, eabq2566 (2022).
29. R. Young, P. L. Read, *Nat. Phys.* **13**, 1135–1140 (2017).
30. Materials and methods are available as supplementary materials.
31. J. Pedlosky, *Geophysical Fluid Dynamics* (Springer, 1987).
32. G. K. Vallis, *Atmospheric and Oceanic Fluid Dynamics: Fundamentals and Large-Scale Circulation* (Cambridge Univ. Press, 2017).
33. P. D. Mininni, D. Rosenberg, R. Reddy, A. Pouquet, *Parallel Comput.* **37**, 316–326 (2011).
34. H.-L. Liu, P. B. Hays, R. G. Roble, *J. Atmos. Sci.* **56**, 2152–2177 (1999).
35. J. Clyne, P. Mininni, A. Norton, M. Rast, *New J. Phys.* **9**, 301 (2007).
36. G. Nastrom, K. Gage, W. Jasperson, *Nature* **310**, 36–38 (1984).
37. T. VanZandt, *Geophys. Res. Lett.* **9**, 575–578 (1982).
38. P. Billant, J.-M. Chomaz, *Phys. Fluids* **13**, 1645–1651 (2001).
39. H. P. Greenspan, *The Theory of Rotating Fluids* (Cambridge Univ. Press, 1968).
40. W. C. Skamarock, S.-H. Park, J. B. Klemp, C. Snyder, *J. Atmos. Sci.* **71**, 4369–4381 (2014).
41. K. S. Gage, G. D. Nastrom, *J. Atmos. Sci.* **43**, 729–740 (1986).
42. D. K. Lilly, *J. Atmos. Sci.* **40**, 749–761 (1983).
43. U. Schumann, *J. Atmos. Sci.* **76**, 3847–3862 (2019).
44. J. Callies, O. Bühler, R. Ferrari, *J. Atmos. Sci.* **73**, 4853–4872 (2016).
45. P. D. Mininni *et al.*, Dataset for large-scale self-organisation in dry turbulent atmospheres, version 1.0, Zenodo (2023); https://doi.org/10.5281/zenodo.8091949.
46. D. Rosenberg, P. Mininni, P. C. Di Leoni, pmininni/GHOST: GHOST master, version 2.0.0, Zenodo (2023); https://doi.org/10.5281/zenodo.8015308.
47. S. Pearse *et al.*, NCAR/VAPOR: Vapor 3.8.1, version 3.8.1, Zenodo (2023); https://doi.org/10.5281/zenodo.7779648.

ACKNOWLEDGMENTS

We thank an anonymous reviewer for the suggestion to calculate data along horizontal tracks, allowing for comparisons with observational data. The simulation output was analyzed on HPC facilities at the École Normale Superieure in Paris (France), at École Centrale de Lyon (PMCS2I) in Ecully (France), and at Departamento de Fisica (FCEN, UBA) in Argentina. **Funding:** Computer resources in Joliot-Curie at CEA were provided by PRACE (research project ID 2020235566) and by GENCI (allocation no. A0110506421). This work was supported by the projects "DYSTURB" (no. ANR-17-CE30-0004) and "EVENTFUL" (no. ANR-20-CE30-0011) funded by the French Agence Nationale de la Recherche (ANR), by the Studienstiftung des deutschen Volkes, by the National Science Foundation (grants DMS-2009563 and DMS-2308337), and by the German Research Foundation (no. 522026592). **Author contributions:** A.A., R.M., P.D.M., and A.v.K. conceived and planned the numerical experiments and wrote the manuscript with input from all authors. A.A. and P.D.M. performed necessary modifications to the GHOST code. A.A. and A.v.K. performed the computations. R.F. and F.F. performed visualizations. All authors analyzed the data and discussed the results. **Competing interests:** The authors declare that they have no competing interests. **Data and materials availability:** Data in all figures are available in the supplementary materials and on Zenodo (*45*). The GHOST code used for the simulations is available on Zenodo (*46*). 3D renderings were done with VAPOR, which is available on Zenodo (*47*).

SUPPLEMENTARY MATERIALS

science.org/doi/10.1126/science.adg8269
Materials and Methods
Supplementary Text
Fig. S1
References (*48*–*56*)
Movie S1

Submitted 24 January 2023; accepted 12 January 2024
10.1126/science.adg8269